J Mater Sci (2023) 58:281–290

Computation & theory

A ferromagnetic hybrid Weyl semimetal in two dimensions: the monolayer $AgCrS_2$

Minghang Li[1,2], Ying Liu[1,2], Xuefang Dai[1,2,*], Guodong Liu[1,2], and Xiaoming Zhang[1,2,*]

[1] State Key Laboratory of Reliability and Intelligence of Electrical Equipment, Hebei University of Technology, Tianjin 300130, China
[2] School of Materials Science and Engineering, Hebei University of Technology, Tianjin 300130, China

Received: 5 August 2022
Accepted: 2 December 2022
Published online: 14 December 2022

ABSTRACT

Topological quantum phases in two-dimensional materials have been a fascinating research topic since the discovery of graphene. Particularly, the topological quantum phases could appear in two-dimensional magnetic systems. However, identifying concrete materials that host topological quantum phases is still a challenge, especially the magnetic ones. In this work, we propose a novel hybrid Weyl semimetal in two dimensions, the monolayer $AgCrS_2$. We show that this material has a stable ferromagnetic ground state with an in-plane magnetic moment. Particularly, it hosts a hybrid of two Weyl nodes close to the Fermi level: one is a double Weyl point, and the other one is type-II linear Weyl point. The features of their band structure could be inferred from the effective models for them. When the spin-orbital coupling is included, the double Weyl point is gapped. In comparison, the type-II linear Weyl nodes on high-symmetry path can be tuned by controlling the orientation of the magnetization direction. To be specific, the magnetization could change locations of type-II linear Weyl nodes and control its stability. Therefore, our results offer a platform to study novel hybrid of Weyl nodes in two-dimensional ferromagnetic system.

Introduction

Two-dimensional (2D) materials and topological quantum states have attracted tremendous attention in recent years [1–5]. A prominent example is graphene, in which the electronic band structure exhibits topologically protected band crossings, denotes as 2D massless Dirac points, at the corner of its Brillouin zone (BZ) [6–9]. Since then, many intriguing physical phenomena, such as ultrahigh mobility and Klein tunneling effect, have been attributed to the topological nature of the nontrivial band crossings [10].

Over the past decades, inspired by the discovery of graphene [11, 12], many 2D topological materials featured by 2D massless Dirac point have been

Handling Editor: Kevin Jones.

Address correspondence to E-mail: xuefangdai@126.com; zhangxiaoming87@hebut.edu.cn

https://doi.org/10.1007/s10853-022-08043-5

predicted theoretically and experimentally [13–16]. Apart from 2D massless Dirac point, other types emergent fermions are also predicted to exist in 2D materials. For example, the monolayer blue phosphorene oxide [17] have been predicted simultaneously to host the double Weyl points and the pseudospin-1 point. The fourfold Dirac point is also proposed in monolayer HfGeTe [18]. In addition, based on the manifold of band crossings, nodal lines are also discovered in many materials, such as monolayer metal-group VI compounds [19], monolayer X_3SiTe_6 (X = Ta, Nb) [20], and monolayer Cu_2Si [21, 22]. Besides, a new classification method for linear dispersion is proposed, which is based on the signs of slopes of the crossing bands. For concreteness, if the crossing bands have opposite signs of slopes, the crossing point is regarded as type-I nodal point. In contrast, if the crossing bands share a sign of slopes, the cone of the crossing point will be completely tipped over, giving rise to a type-II nodal point [23–27]. Until now, the type-II nodal point has been proposed in a few 2D materials, such as WTe_2 [28], $MoTe_2$ [29], Ta_3S_2 and $TaIrTe_4$ [30, 31]. So far, majority of the proposed materials are nonmagnetic, and the magnetic 2D materials with emergent fermions are still limited, especially the materials with coexistence of different types of fermions.

Most recently, the fully spin-polarized hybrid Weyl semimetal, the ferromagnetic monolayer Cr_2C, is identified [32]. This material is a new type Weyl semimetal, in which one of Weyl point is type-I, while the other one is type-II. Is it possible to realize a coexistence of type-I double Weyl and type-II linear Weyl points, especially in magnetic systems?

Our work answers this question in the affirmative. We reveal a 2D material as an example of a new type of hybrid Weyl semimetal. Via the first-principles calculation and theoretical analysis, we predict that the ferromagnetic monolayer $AgCrS_2$ simultaneously hosts a double Weyl point at the Γ point and a type-II linear Weyl point on the high-symmetry path. We demonstrate its stability in the monolayer form. Importantly, its bulk form has been experimentally synthesized by chemical vapor transport (CVT) [33], exhibiting a layered structure. Then, its monolayer form is obtained by exfoliation from the bulk. Since the monolayer $AgCrS_2$ exhibits a ferromagnetic ground state, the hybrid of Weyl points could be spin-polarized. Moreover, considering the stability of Weyl points, we show that the double Weyl point is protected by a threefold rotation symmetry, and the type-II linear Weyl points are stabilized by a mirror symmetry. Then, based on the symmetry analysis, the effective models are constructed to describe the double Weyl and type-II linear Weyl points. We further show that, under the symmetry breaking, this hybrid of Weyl points shall undergo a phase transition. For concreteness, the double Weyl point could transform into a pair of type-I linear Weyl points with breaking the threefold rotation symmetry. On the other hand, the type-II linear Weyl can be tuned by controlling the magnetization. Therefore, our work provides an example to study a new type of hybrid Weyl semimetals in 2D.

Computational method

This work was carried out using first-principles calculations using the Vienna ab initio simulation software package [34, 35]. The correlation potential was selected as the generalized gradient approximation (GGA), and Perdew–Burke–Ernzerhof (PBE) was adopted [36]. Set the plane wave cutoff energy to 520 eV. For Brillouin area sampling, Monkhorst–Pack K-mesh was used and the size was set to $9 \times 9 \times 1$. The convergence criterion of energy is 10^{-6} eV, and the convergence criterion of force is 0.01 eV/Å. The long-range van der Waals interactions are account by using the DFT-D2 method [37]. In order to explain the strongly correlated interaction of transition metal element Cr atom in $AgCrS_2$, the GGA + U method was adopted [38], and the effective U value was selected as 1 eV. To be noted, changing the U values in the range of 0–4 eV will not change the conclusion of the work. Topological surface states are calculated by using the WANNIERTOOLS software package [39].

Results and discussion

Crystal structure, magnetism and topological structure

The lattice structure and Brillouin zone of $AgCrS_2$ are shown in Fig. 1a, b, respectively. For the top and side views, one could obtain that it possesses hexagonal atomic layers: the plane of Cr atoms sandwiched by two layers of S atoms with an ABC-type stacking,

then sandwich the Ag atoms layer. The lattice structure belongs to space group *P3m1* and has a point group C_{3v}. The primitive cell is indicated by the shadow region in Fig. 1a, with one Ag atom, two Cr atoms and four S atoms. By optimizing the lattice constant, as shown in Fig. 1c, the most stable lattice constant is a = b = 3.4281 Å, with which the system has the lowest energy. In addition, its thermal stability can be inferred from Fig. 1d calculated by the ab initio molecular dynamics (AIMD). It shows good stability around the room temperature. Importantly, its bulk form has been experimentally synthesized by chemical vapor transport (CVT) exhibiting a layered structure. Interesting, bulk $AgCrS_2$ is an antiferromagnetic semiconductor (See Supporting Information). In previous reports, we find that the $NaCrS_2$ family with the same structure shows similar results as $AgCrS_2$, namely the bulk is antiferromagnetic, while the monolayer shows intrinsic ferromagnetism. [40] Then, its monolayer form is obtained by exfoliation from the bulk [33]. We further calculate the exfoliation energy of monolayer $AgCrS_2$, and the exfoliation energy is 1.27 (J/m^2) (as shown in Fig. S5). Compared with the exfoliation energy of other 2D materials, such as graphene (0.37 J/m^2) [41], GeP_3 (1.14 J/m^2) [42], InP_3 (1.32 J/m^2) [43], Ga_2N (1.09 J/m^2) [44], ReS_2 (2.15 J/m^2) [45], the monolayer $AgCrS_2$ is feasible to be exfoliated from the bulk structure.

Before studying its electronic band structure, it is essential to study its magnetic ground state. The magnetic ground state of monolayer $AgCrS_2$ was evaluated by constructing nonmagnetic (NM), ferromagnetic (FM) and antiferromagnetic (AFM) configurations including (AFM1, AFM2, AFM3) in 2 × 2 × 1 supercell. We compared the energies of different magnetic configurations at different U values, and the results are shown in Fig. S3 and Fig. S4. Here, the energy of FM state is set as reference energy. We can find that the FM state always has the lowest energy at different U values. Therefore, the FM state is most energetically stable in all magnetic configurations. We find that the magnetic moment is closest to the experimental value [46, 47] when set the U value as 1 eV (see Fig. S4). Therefore, the U value for Cr is chosen as 1 eV in the following calculation.

Then, it is important to determine the direction of the magnetic moment. The magnetic anisotropy energy (MAE) is performed via DFT + U + SOC calculation. Here, the calculations include the spin rotating in *X*–*Y* and *X*–*Z* planes, as shown in Fig. 2a,

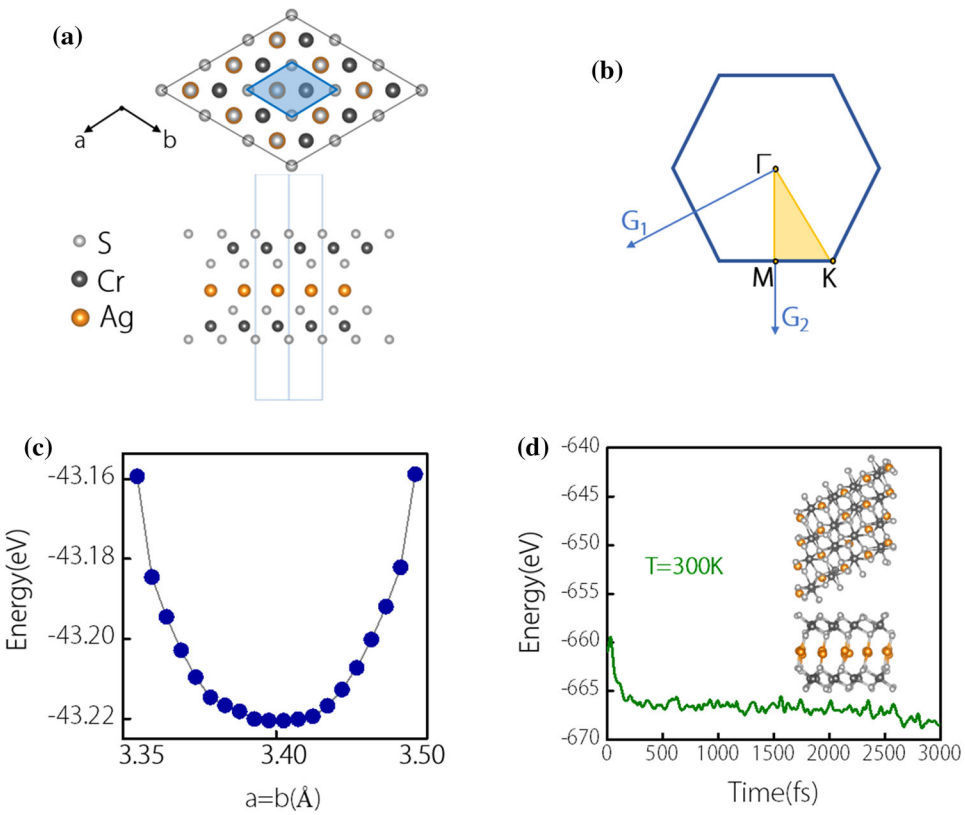

Figure 1 **a** Top view and side view of two-dimensional material $AgCrS_2$ monolayer structure. **b** The first Brillouin zone of monolayer $AgCrS_2$, marked with high-symmetry points. **c** The schematic diagram of optimized lattice constant. **d** Total potential energy fluctuations of the $AgCrS_2$ monolayer during AIMD simulations at 300 K, and the insets show the final state of the structure after AIMD simulation.

b, respectively. In comparison, the easy axis of magnetic moment is in-plane (as shown in Fig. 2c), and the energy of this state is lower (the maximal value is up to 0.53 meV) than that of the out-of-plane magnetization. In addition, its magnetic moment is isotropic in the X–Y plane. One may note that the energy difference between in-plane and out-of-plane is tiny, such that the magnetic moment could be easily changed under external fields. Based on Heisenberg model [48, 49], namely $H = -\sum_{i\neq j} J_{ij} S_i \cdot S_j - \frac{K_N}{2}\sum_i \left(S_i^z\right)^2$, where i and j represent the sites of Cr atoms, J_{ij} represents the exchange interaction strength, and K_N represents the magnetic anisotropy. The magnetic moment of Cr atom 3 μ_B for monolayer $AgCrS_2$. Based on DFT calculations, we calculated the exchange constants for the nearest- and next-nearest-neighbor interactions of monolayer $AgCrS_2$ are J_1 = 0.176181 meV and J_2 = 1.756597 meV, respectively.

After determining the magnetic configuration, we begin to study its electronic band structure and corresponding symmetry protections. Given the ferromagnetic ground state, we plot the electronic band structure for spin-up and spin-down states in Fig. 3a, b, respectively. In comparison, one can obtain that the low-energy states are mainly contributed by states of spin-up. The zoom-in image for the spin-up states in the low-energy region is given in Fig. 4a, from which one can observe that a double Weyl point appears at the Γ point. Remarkably, the double Weyl point lies in the gap of spin-down states, exhibiting a fully spin-polarized property. Meanwhile, a type-II linear Weyl point appears on path Γ–M. Notably, the type-II Weyl point is another crossing point of the crossing bands for the double Weyl point, thus constructing a hybrid of Weyl nodes: one is a double Weyl point, and the other one is a type-II linear Weyl point. Their dispersion features can be further demonstrated by their 3D energy band structures in Fig. 4b. Indeed, the double Weyl point has an upright Weyl cone, while the cone of the type-II linear Weyl point is tipped over.

Furthermore, due to the presence of C_{3z}, there are totally three pairs of type-II Weyl points in the first Brillouin zone, and their distribution is given in the right panel of Fig. 4c. The presence of nontrivial band crossing points is accompanied by edge states. We plot the surface spectrum in [100] direction in Fig. 4c. One can observe that there are two Fermi arcs stemming from the projections of type-II linear Weyl points, because each projected point is an overlapping of two linear Weyl points. Regarding the projection of the double Weyl point, two Fermi arcs emanate from this projection (see in Fig. 4d). It is worth pointing out that the double Weyl point lies in the gap of the spin-down channel, Fermi arcs are far from other trivial bands. This makes them more accessible in experiments.

Effective models

In the following, we turn our attention to the symmetry protection for the double Weyl point and the type-II linear Weyl point. As aforementioned, the

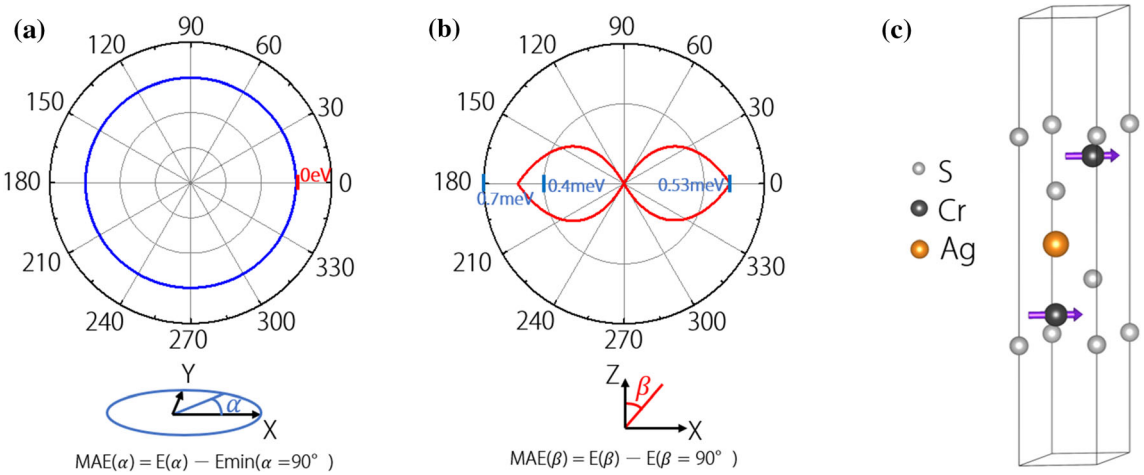

Figure 2 The magnetic anisotropy energy (MAE) by rotating the spin within **a** XY plane and **b** XZ plane, respectively. **c** Schematic diagram of ferromagnetic structure of monolayer $AgCrS_2$. (The direction of purple arrow is magnetic moment direction of Cr atom).

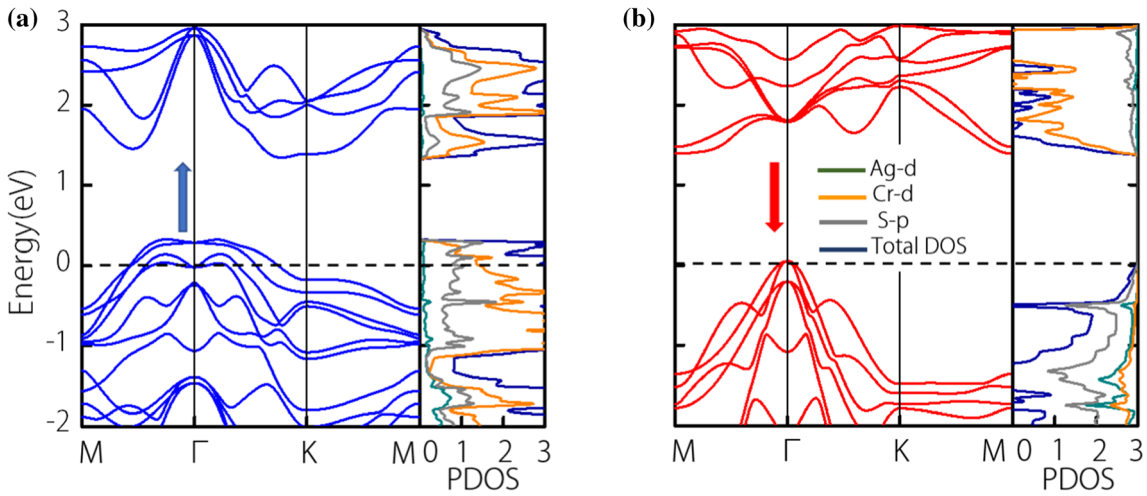

Figure 3 The electronic band structure and the corresponding projection state density (PDOS) in **a** spin up channel and **b** spin down channel of monolayer $AgCrS_2$ in the absence of SOC.

point group at Γ point is C_{3v}, which is generated by a threefold rotation symmetry C_{3z} and a mirror symmetry M_y. For this point group, there is a 2D irreducible representation, namely, E, which determines a double degeneracy. Such that the double degenerate point at Γ point is an essential band crossing. After a unitary transformation, we can write the matrix representations for the generating elements in the eigenstates of C_{3z}, to be specific,

$$C_{3z} = -\frac{1}{2}\sigma_0 - i\frac{\sqrt{3}}{2}\sigma_z, M_y = \sigma_y. \quad (1)$$

Here, σ is the Pauli matrix. In addition, since the double Weyl point only appears in spin-up channel at the Γ point, it also enjoys an effective time-reversal symmetry, with $T = \sigma_x K$, and K is the complex conjugation. Constrained by these operations, the effective model for the double Weyl point is written as

$$H_{\mathrm{DW}}(k_x, k_y) = c_0 + c_1\left(k_x^2 + k_y^2\right) + \left[\alpha k_-^2 \sigma_+ + h.c.\right], \quad (2)$$

where c is real parameter and α is an imaginary parameter. Such an effective Hamiltonian leads to a quadratic dispersion, with energy eigenvalues

$$E = c_0 + c_1\left(k_x^2 + k_y^2\right) \pm |\alpha|^2\left(k_x^2 + k_y^2\right), \quad (3)$$

in line with our DFT calculation. Here, it is necessary to mention that the essential symmetry for the stability of the double Weyl point is C_{3z}, which have been discussed in Ref. [50]. When breaking C_{3z}, a double Weyl point transforms into a pair of 2D linear Weyl points, as demonstrated in Fig. 4e, f.

Turn to the type-II Weyl points on Γ–M, their stability is ensured by M_y. On this path, due to the absence of T, the linear term proportional to identity matrix could be allowed. Together with M_y, the linear term $a_1 k_x$ could exist on this path. Interestingly, this $a_1 k_x$ could play a role in tilting the Weyl cone. For concreteness, the crossing bands are characterized by opposite eigenvalues. Considering the mirror symmetry $M_y = \sigma_y$, a low-energy model around the type-II Weyl point can be given by,

$$H_{\Gamma-M}(k_x, k_y) = a_0 + a_1 k_x + (a_2 k_x - \Delta)\sigma_y + k_y(a_3\sigma_x + a_4\sigma_z). \quad (4)$$

Here, a is real parameter. According to Eq. (4), there is indeed a crossing point at position $\boldsymbol{k}_0 = \left(\frac{\Delta}{a_2}, 0\right)$, and the dispersion around this point is linear. Particularly, the Weyl cone is determined by the titled term $a_1 k_x$, when $|a_1| > |a_2|(|a_1| < |a_2|)$, the effective model indicates a type-II (type-I) Weyl point. In our work, one should have $|a_1| > |a_2|$, thus leading to a type-II Weyl point.

When considering the spin-orbital coupling (SOC), the presence of in-plane magnetic moment may destroy the double Weyl point due to the breaking of C_{3z}. For example, the magnetization in [100] direction gap the double Weyl point (see Supporting Information). On contrast, the type-II linear Weyl point could be tuned by controlling the orientation of magnetization. To be specific, if the magnetization is on y-axis, with $m_y = M\sigma_y$, the mirror M_y allows its presence in Eq. (4) due to $[M_y, m_y] = 0$. Consequently,

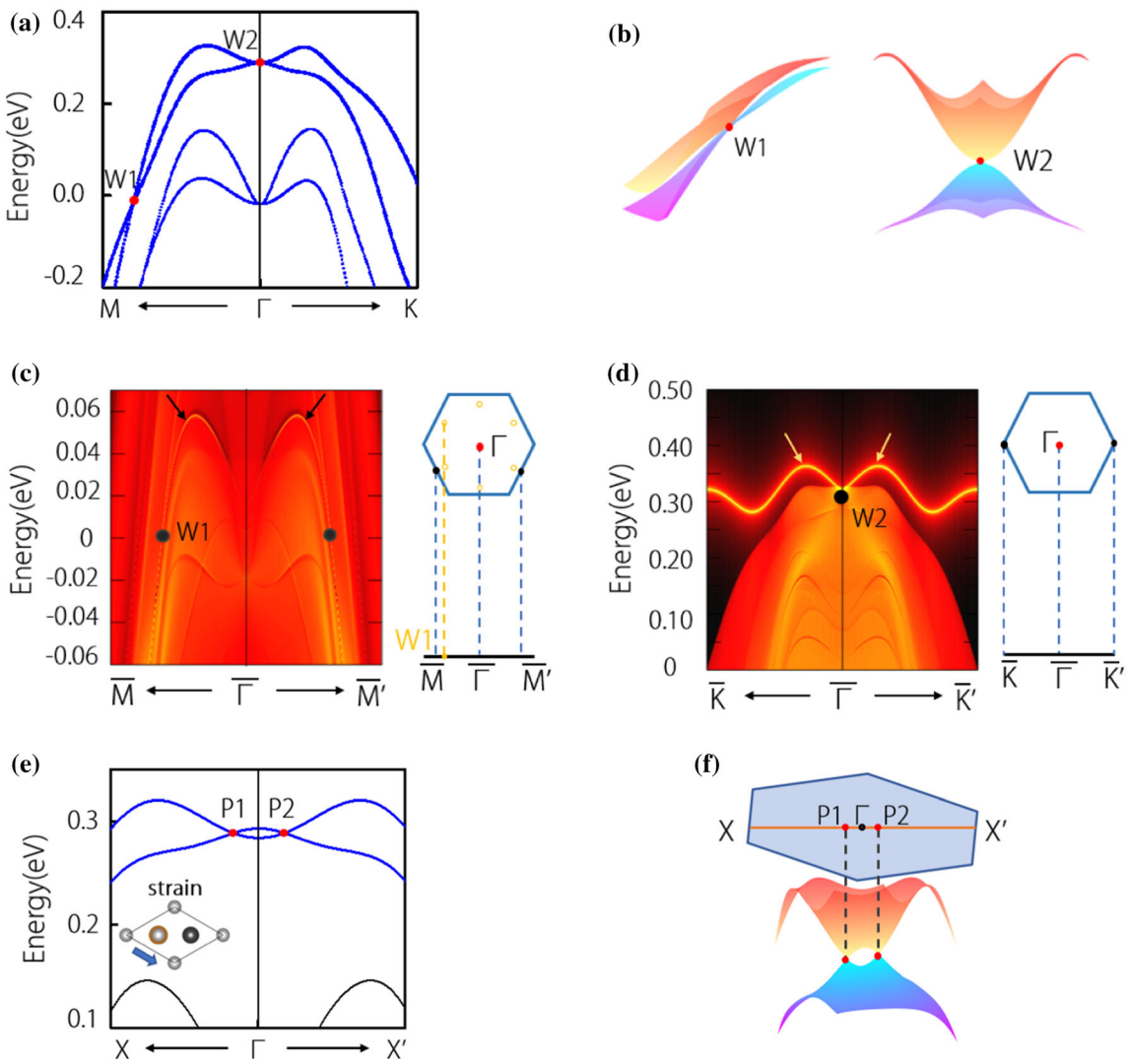

Figure 4 **a** Enlarged view of $AgCrS_2$ electron band structure along the M–Γ–K path. **b** The enlarged image of the 3D band dispersion of the type-II Weyl point (labeled W1) and the quadratic Weyl point (labeled W2) along the M–Γ path. The edge spectrum corresponding to **c** W1 and **d** W2 of monolayer $AgCrS_2$. **e** The electronic band structure of monolayer $AgCrS_2$ along the path X–Γ–X′ at 0.15% uniaxial stress. **f** 3D dispersion of two Weyl points P1 and P2 along the X–Γ–X′ path.

the presence of this term only changes the position of the type-II Weyl point, from $\boldsymbol{k}_0$ to $\left(\frac{\Delta - M}{c_2}, 0\right)$. It could be demonstrated in Fig. 5b. In another word, m_y could be used to control the position of type-II Weyl points. When the magnetization direction removes from this direction, the type-II linear Weyl point on path Γ–M is gapped, as shown in Fig. 5a. The maximal gap is 11.11 meV with magnetization in x-axis, with $m_x = M\sigma_x$, as indicated in Fig. 5c. After a 60-degree rotation, the crossing point reappears, as shown in Fig. 5d. Because of the threefold rotation symmetry and mirror symmetry, there are six equal regions, as shown in Fig. 5a. Therefore, the presence of magnetization also could permit the presence of type-II linear Weyl points in the 2D $AgCrS_2$. Particularly, the magnetization can be used to manipulate the type-II Weyl points.

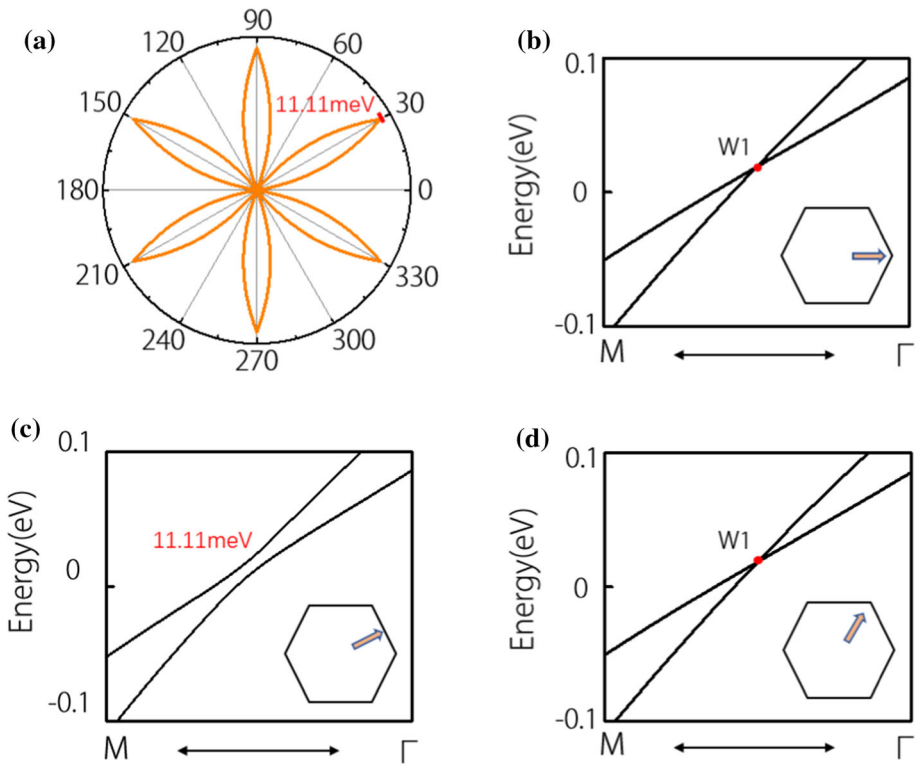

Figure 5 **a** The flowered curve (yellow line) shows the relationship between the band gap at W1 point and azimuth in the in-plane magnetization direction, where the polar radius represents the band gap value. The band structures near W1 point under SOC when the azimuth in the in-plane magnetization direction is **b** 0 degree, **c** 30 degree and **d** 60 degree.

Conclusion

We have revealed that the 2D $AgCrS_2$ hosts a hybrid of two Weyl points: one is double Weyl point, and the other one is type-II linear Weyl point. Remarkably, such a hybrid of Weyl nodes only appears in one spin-channel; thus, the Weyl nodes are fully spin-polarized. Based on the symmetry analysis, we construct the effective models for the double Weyl and type-II linear Weyl points. We also find that the essential symmetry for the double Weyl point is C_{3z}. Breaking the threefold rotation symmetry, the double Weyl point vanishes, transforming into a pair of linear Weyl points. Regarding the stability of type-II Weyl points, the mirror symmetry M_y is significant for their existence. Such that the stabilities of double Weyl point and type-II Weyl point are separately protected by symmetries at Γ point and on Γ–M path. Particularly, the type-II linear Weyl points can be controlled by tuning the orientation of magnetization: if the magnetic moment is invariant under M_y, say m_y, the type-II Weyl point still persists in $AgCrS_2$, but the double Weyl point is gapped. In comparison, the magnetization in a generic direction in the plane, the type-II Weyl point and double Weyl point are expected to be simultaneously destroyed. In conclusion, our work provides an excellent platform for exploring the intriguing physics of 2D magnetic hybrid Weyl semimetals, which can lead to potential applications in nanoscale spintronics.

Acknowledgements

This work is supported by the National Natural Science Foundation of China (Grants No. 11904074). The work is funded by the Science and Technology Project of the Hebei Education Department, the Nature Science Foundation of Hebei Province, the S&T Program of Hebei (No. A2021202012), the Overseas Scientists Sponsorship Program by Hebei Province (C20210330), and the fund from the State Key Laboratory of Reliability and Intelligence of Electrical Equipment of Hebei University of Technology (No. EERI_PI2020009). One of the authors (X.M.Z.) acknowledges financial support from the Young Elite Scientists Sponsorship Program by Tianjin.

Declarations

Conflict of interest The authors declare that they have no known competing financial interests or

personal relationships that could have appeared to influence the work reported in this paper.

Supplementary Information: The online version contains supplementary material available at https://doi.org/10.1007/s10853-022-08043-5.

References

[1] Ezawa M (2012) Valley-polarized metals and quantum anomalous Hall effect in silicene. Phys Rev Lett 109:055502. https://doi.org/10.1103/PhysRevLett.109.055502

[2] Ezawa M (2013) Spin valleytronics in silicene: quantum spin Hall–quantum anomalous Hall insulators and single-valley semimetals. Phys Rev B 87:155415. https://doi.org/10.1103/PhysRevB.87.155415

[3] Zhang L, Bampoulis P, Rudenko AN, Yao Q, van Houselt A, Poelsema B, Katsnelson MI, Zandvliet HJW (2016) Structural and electronic properties of germanene on MoS_2. Phys Rev Lett 116:256804. https://doi.org/10.1103/PhysRevLett.116.256804

[4] Amlaki T, Bokdam M, Kelly PJ (2016) Z_2 invariance of Germanene on MoS_2 from first principles. Phys Rev Lett 116:256805. https://doi.org/10.1103/PhysRevLett.116.256805

[5] Tang P, Chen P, Cao W, Huang H, Cahangirov S, Xian L, Xu Y, Zhang SC, Duan W, Rubio A (2014) Stable two-dimensional dumbbell stanene: a quantum spin Hall insulator. Phys Rev B 90:121408. https://doi.org/10.1103/PhysRevB.90.121408

[6] De Martino A, Dell'Anna L, Egger R (2007) Magnetic confinement of massless Dirac fermions in graphene. Phys Rev Lett 98:066802. https://doi.org/10.1103/PhysRevLett.98.066802

[7] Park CH, Yang L, Son YW, Cohen ML, Louie SG (2008) New generation of massless Dirac fermions in graphene under external periodic potentials. Phys Rev Lett 101:126804. https://doi.org/10.1103/PhysRevLett.101.126804

[8] Zhou XF, Dong X, Oganov AR, Zhu Q, Tian Y, Wang HT (2014) Semi-metallic two-dimensional boron allotrope with massless Dirac fermions. Phys Rev Lett 112:085502. https://doi.org/10.1103/PhysRevLett.112.085502

[9] Nomura K, MacDonald AH (2007) Quantum transport of massless Dirac fermions. Phys Rev Lett 98:076602. https://doi.org/10.1103/PhysRevLett.98.076602

[10] Castro Neto AH, Guinea F, Peres NMR, Novoselov KS, Geim AK (2009) The electronic properties of graphene. Rev Mod Phys 81:109. https://doi.org/10.1103/RevModPhys.81.109

[11] Novoselov KS, Geim AK, Morozov SV, Zhang DJ, Dubonos SV, Grigorieva IV, Firsov AA (2004) Electric field effect in atomically thin carbon films. Science 306:666–669. https://doi.org/10.1126/science.1102896

[12] Zhou SY, Gweon GH, Graf J, Fedorov AV, Spataru CD, Diehl RD, Kopelevich Y, Leel DH, Steven G, Lanzara A (2006) First direct observation of Dirac fermions in graphite. Nature Phys 2:595–599. https://doi.org/10.1038/nphys393

[13] Young SM, Kane CL (2015) Dirac semimetals in two dimensions. Phys Rev Lett 115:126803. https://doi.org/10.1103/PhysRevLett.115.126803

[14] Fashandi H, Ivády V, Eklund P, Spetz AL, Katsnelson MI, Abrikosov IA (2015) Dirac points with giant spin-orbit splitting in the electronic structure of two-dimensional transition-metal carbides. Phys Rev B 92:155142. https://doi.org/10.1103/PhysRevB.92.155142

[15] Wu H, Qian Y, Du Z, Zhu R, Kan E, Deng K (2017) Prediction of another semi-metallic silicene allotrope with Dirac fermions. Phys Lett A 381:3754–3759. https://doi.org/10.1016/j.physleta.2017.09.049

[16] Meng W, Zhang X, Yu W, Liu Y, Tian L, Dai X, Liu G (2021) Multiple Weyl fermions and tunable quantum anomalous Hall effect in 2D half-metal with huge spin-related energy gap. Appl Surf Sci 551:149390. https://doi.org/10.1016/j.apsusc.2021.149390

[17] Zhu L, Wang SS, Guan S, Liu Y, Zhang T, Chen G, Yang SA (2016) Blue phosphorene oxide: strain-tunable quantum phase transitions and novel 2D emergent fermions. Nano Lett 16:6548–6554. https://doi.org/10.1021/acs.nanolett.6b03208

[18] Guan S, Liu Y, Yu ZM, Wang SS, Yao Y, Yang SA (2017) Two-dimensional spin-orbit Dirac point in monolayer HfGeTe. Phys Rev Mater 1:054003. https://doi.org/10.1103/PhysRevMaterials.1.054003

[19] Jin YJ, Wang R, Zhao JZ, Du YP, Zheng CD, Gan LY, Liu JF, Xu H, Tong S (2017) The prediction of a family group of two-dimensional node-line semimetals. Nanoscale 9:13112–13118. https://doi.org/10.1039/C7NR03520A

[20] Li S, Liu Y, Wang SS, Yu ZM, Guan S, Sheng XL, Yao Y, Yang SA (2018) Nonsymmorphic-symmetry-protected hourglass Dirac loop, nodal line, and Dirac point in bulk and monolayer X_3SiTe_6 (X= Ta, Nb). Phys Rev B 97:045131. https://doi.org/10.1103/PhysRevB.97.045131

[21] Feng B, Fu B, Kasamatsu S, Ito S, Cheng P, Liu CC, Feng Y, Wu S, Mahatha SK, Sheverdyaeva P, Moras P, Arita M, Sugino O, Chiang TC, Shimada K, Miyamoto K, Okuda T, Wu K, Chen L, Yao Y, Matsuda I (2017) Experimental realization of two-dimensional Dirac nodal line fermions in

monolayer Cu_2Si. Nat Comm 8:1007. https://doi.org/10.1038/s41467-017-01108-z

[22] Yang LM, Bacic V, Popov IA, Boldyrev AI, Heine T, Frauenheim T, Ganz E (2015) Two-dimensional Cu_2Si monolayer with planar hexacoordinate copper and silicon bonding. J Am Chem Soc 137:2757–2762. https://doi.org/10.1021/ja513209c

[23] Zhang X, Jin L, Dai X, Liu G (2017) Topological type-II nodal line semimetal and Dirac semimetal state in stable kagome compound Mg_3Bi_2. J Phys Chem Lett 8:4814–4819. https://doi.org/10.1021/acs.jpclett.7b02129

[24] Sharma G, Goswami P, Tewari S (2017) Chiral anomaly and longitudinal magnetotransport in type-II Weyl semimetals. Phys Rev B 96:045112. https://doi.org/10.1103/PhysRevB.96.045112

[25] He T, Zhang X, Wang L, Liu Y, Dai X, Wang L, Liu G (2021) Ideal fully spin-polarized type-II nodal line state in half-metals X_2YZ_4 (X= K, Cs, Rb, Y=Cr, Cu, Z= Cl, F). Mater Today Phys 17:100360. https://doi.org/10.1016/j.mtphys.2021.100360

[26] Meng W, Zhang X, Liu Y, Dai X, Liu G (2021) Antiferromagnetism caused by excess electrons and multiple topological electronic states in the electride $Ba_4Al_5{\cdot}e^-$. Phys Rev B 104:195145. https://doi.org/10.1103/PhysRevB.104.195145

[27] Meng W, Zhang X, He T, Jin L, Dai X, Liu Y, Liu G (2020) Ternary compound HfCuP: an excellent Weyl semimetal with the coexistence of type-I and type-II Weyl nodes. J Adv Res 24:523–528. https://doi.org/10.1016/j.jare.2020.05.026

[28] Soluyanov AA, Gresch D, Wang Z, Wu Q, Troyer M, Dai X, Bernevig BA (2015) Type-ii Weyl semimetals. Nature 527:495–498. https://doi.org/10.1038/nature15768

[29] Wang Z, Gresch D, Soluyanov AA, Xie W, Kushwaha S, Dai X, Troyer M, Cava RJ, Bernevig BA (2016) $MoTe_2$: a type-II Weyl topological metal. Phys Rev Lett 117:056805. https://doi.org/10.1103/PhysRevLett.117.056805

[30] Koepernik K, Kasinathan D, Efremov DV, Khim S, Borisenko S, Büchner B, van den Brink J (2016) $TaIrTe_4$: a ternary type-II Weyl semimetal. Phys Rev B 93:201101(R). https://doi.org/10.1103/PhysRevB.93.201101

[31] Chang G, Xu SY, Sanchez DS, Huang SM, Lee CC, Chang TR, Bian G, Zheng H, Belopllski I, Alidoust N, Jeng HT, Bansil A, Lin H, Hasan MZ (2016) A strongly robust type II Weyl fermion semimetal state in Ta_3S_2. Sci adv 2:e1600295. https://doi.org/10.1126/sciadv.1600295

[32] Meng W, Zhang X, Liu Y, Wang L, Dai X, Liu G (2021) Two-dimensional Weyl semimetal with coexisting fully spin-polarized type-I and type-II Weyl points. Appl Surf Sci 540:148318. https://doi.org/10.1016/j.apsusc.2020.148318

[33] Peng J, Liu Y, Lv H, Li Y, Lin Y, Su Y, Wu J, Liu H, Guo Y, Zhuo Z, Wu X, Wu C, Xie Y (2021) Stoichiometric two-dimensional non-van der Waals $AgCrS_2$ with superionic behavior at room temperature. Nat Chem 13:1235–1240. https://doi.org/10.1038/s41557-021-00800-4

[34] Kresse G, Joubert D (1999) From ultrasoft pseudopotentials to the projector augmented-wave method. Phys Rev B 59:1758. https://doi.org/10.1103/PhysRevB.59.1758

[35] Blochl PE (1994) Projector augmented-wave method. Phys Rev B 50:17953. https://doi.org/10.1103/PhysRevB.50.17953

[36] Perdew JP, Burke K, Ernzerhof M (1996) Generalized gradient approximation made simple. Phys Rev Lett 77:3865. https://doi.org/10.1103/PhysRevLett.77.3865

[37] Grimme S (2006) Semiempirical GGA-type density functional constructed with a long-range dispersion correction. J Comput Chem 27:1787–1799. https://doi.org/10.1002/jcc.20495

[38] Anisimov VI, Zaanen J, Andersen OK (1991) Band theory and Mott insulators: Hubbard U instead of Stoner I. Phys Rev B 44:943. https://doi.org/10.1103/PhysRevB.44.943

[39] Wu QS, Zhang SN, Song HF, Troyer M, Soluyanov AA (2018) WannierTools: an open-source software package for novel topological materials. Comput Phys Commun 224:405–416. https://doi.org/10.1016/j.cpc.2017.09.033

[40] Xu W, Ali S, Jin Y, Wu X, Xu H (2020) Intrinsic ferromagnetic semiconductors in two-dimensional alkali-based chromium chalcogenides. ACS Appl Electron Mater 2:3853–3858. https://doi.org/10.1021/acsaelm.0c00686

[41] Wang W, Dai S, Li X, Yang J, Srolovitz DJ, Zheng Q (2015) Measurement of the cleavage energy of graphite. Nat Commun 6:1–7. https://doi.org/10.1038/ncomms8853

[42] Jing Y, Ma Y, Li Y, Heine T (2017) GeP3: a small indirect band gap 2D crystal with high carrier mobility and strong interlayer quantum confinement. Nano Lett 17:1833–1838. https://doi.org/10.1021/acs.nanolett.6b05143

[43] Miao N, Xu B, Bristowe NC, Zhou J, Sun Z (2017) Tunable magnetism and extraordinary sunlight absorbance in indium triphosphide monolayer. J Am Chem Soc 139:11125–11131. https://doi.org/10.1103/PhysRevLett.116.256804

[44] Zhao S, Li Z, Yang J (2014) Obtaining two-dimensional electron gas in free space without resorting to electron doping: an electride based design. J Am Chem Soc 136:13313–13318. https://doi.org/10.1021/ja5065125

[45] Wang H, Liu E, Wang Y, Wan B, Ho CH, Miao F, Wan XG (2017) Cleavage tendency of anisotropic two-dimensional materials: ReX_2 (X= S, Se) and WTe_2. Phys Rev B 96:165418. https://doi.org/10.1103/PhysRevB.96.165418

[46] Ushakov AV, Kukusta DA, Yaresko AN, Khomskii DI (2013) Magnetism of layered chromium sulfides $MCrS_2$ (M=

Li, Na, K, Ag, and Au): a first-principles study. Phys Rev B 87:014418. https://doi.org/10.1103/PhysRevB.87.014418

[47] Damay F, Martin C, Hardy V, Andre G, Petit S, Maignan A (2011) Magnetoelastic coupling and unconventional magnetic ordering in the multiferroic triangular lattice $AgCrS_2$. Phys Rev B 83:184413. https://doi.org/10.1103/PhysRevB.83.184413

[48] Evans RF, Fan WJ, Chureemart P, Ostler TA, Ellis MO, Chantrell RW (2014) Atomistic spin model simulations of magnetic nanomaterials. J Phys Condens Matter 26:103202. https://doi.org/10.1088/0953-8984/26/10/103202

[49] Zhu Y, Xu S, Chen T, Cheng X, Fang L, Hu S, Hu T, Jia F, Gao H, Ren W (2022) Prediction of 2D ferromagnetic metal VNI monolayer with tunable topological properties. J Appl Phys 132:183913. https://doi.org/10.1063/5.0107680

[50] Yu WW, Liu Y, Meng W, Liu H, Gao J, Zhang X, Liu G (2022) Phononic higher-order nodal point in two dimensions. Phys Rev B 105:035429. https://doi.org/10.1103/PhysRevB.105.035429